

Correction for Partial Volume Effects in PET: Principle and Validation

Olivier G. Rousset, Yilong Ma and Alan C. Evans

McConnell Brain Imaging Center, Montréal Neurological Institute, McGill University, Montréal, Québec, Canada

The accuracy of PET for measuring regional radiotracer concentrations in the human brain is limited by the finite resolution capability of the scanner and the resulting partial volume effects (PVEs). We designed a new algorithm to correct for PVEs by characterizing the geometric interaction between the PET system and the brain activity distribution. **Methods:** The partial volume correction (PVC) algorithm uses high-resolution volumetric MR images correlated with the PET volume. We used a PET simulator to calculate recovery and cross-contamination factors of identified tissue components in the brain model. These geometry-dependent transfer coefficients form a matrix representing the fraction of true activity from each distinct brain region observed in any given set of regions of interest. This matrix can be inverted to correct for PVEs, independent of the tracer concentrations in each tissue component. A sphere phantom was used to validate the simulated point-spread function of the PET scanner. Accuracy and precision of the PVC method were assessed using a human basal ganglia phantom. A constant contrast experiment was performed to explore the recovery capability and statistic error propagation of PVC in various noise conditions. In addition, a dual-isotope experiment was used to evaluate the ability of the PVC algorithm to recover activity concentrations in small structures surrounded by background activity with a different radioactive half-life. This models the time-variable contrast between regions that is often seen in neuroreceptor studies. **Results:** Data from the three-dimensional brain phantom demonstrated a full recovery capability of PVC with less than 10% root mean-square error in terms of absolute values, which decreased to less than 2% when results from four PET slices were averaged. Inaccuracy in the estimation of ^{18}F tracer half-life in the presence of ^{11}C background activity was in the range of 25%–50% before PVC and 0%–6% after PVC, for resolution varying from 6 to 14 mm FWHM. In terms of noise propagation, the degradation of the coefficient of variation after PVC was found to be easily predictable and typically on the order of 25%. **Conclusion:** The PVC algorithm allows the correction for PVEs simultaneously in all identified brain regions, independent of tracer levels.

Key Words: correction; partial volume effects; PET; simulation; regions of interest

J Nucl Med 1998; 39:904–911

Despite the wide range of tracers available, the relatively poor spatial resolution of PET has always been a major limiting factor for the accuracy of quantitative studies, particularly compartmental analysis of radioligand kinetics. The direct consequence of limited resolution is the loss of signal for structures partially occupying the point-spread function (PSF) of the scanner, i.e., with dimensions smaller than about 2–3 times its FWHM (1–3). This effect was first estimated by the overlap of the scanner's PSF with the object being imaged and was referred to as its recovery coefficient (RC), i.e., the ratio of observed to true activity in the absence of surrounding activity (1,2). Although the partial volume effect originally referred to

the loss of signal due to the limited axial extent of the object with respect to the axial PSF or slice thickness (4), this concept became more general and came to also designate the partial overlap of the object with the transverse component of the PSF (5,6). The reciprocal effect of poor spatial resolution is the contamination of activity from neighboring tissues or spillover effect (3,6–8). However, partial volume effects (PVEs) usually incorporate both aspects of poor spatial resolution (partial volume and spillover).

In quantitative studies, PVEs introduce distortions that depend on tracer distribution, both in the targeted region and in adjacent tissues (8,9). This changes both the magnitude and the shape of the time-activity curves (TACs), resulting in typical errors of 50% in estimated rate constants for metabolism and transfer of tracer between compartments (10).

Physical phantom studies are commonly used to characterize the nature and magnitude of PVEs (1–3,11–14). A second class of methods is based on computer-aided simulation of PET scanner resolution and digitized images of brain anatomy. This was first introduced using post mortem brain slices (15–17) and was further developed with images created by anatomical imaging devices (18). In vivo correction approaches based on high-resolution MR or transmission CT were first developed to correct for brain activity dilution by cerebrospinal fluid (CSF) spaces, in two (19) and in three dimensions (20). Later, a method accounting for white matter contribution to gray matter measurements was developed (21). This approach has been further extended to allow for a more heterogeneous tracer distribution in gray matter, by including a distinct volume of interest for subcortical gray structures (22).

We previously introduced a correction based on regional estimates of the contribution of each functionally distinct brain region (8,10). In this work, the basic principles of the partial volume correction (PVC) algorithm are presented, along with validation results from a multiple-sphere phantom and a realistic three-dimensional brain phantom scanned on the PC-2048 system at the Montréal Neurological Institute and the PC-4096 system at Johns Hopkins Hospital (Baltimore, MD).

MATERIALS AND METHODS

Theory

Providing that the linear characteristics of PET are preserved for the levels and distributions of activity encountered, the PET image $g(\mathbf{r})$ represents the weighted integration of the activity distribution $f(\mathbf{r})$ present in the field of view (FOV), by the response function of the PET system in terms of its PSF $h(\mathbf{r})$:

$$g(\mathbf{r}) = \int_{\text{FOV}} f(\mathbf{r}')h(\mathbf{r}, \mathbf{r}') d\mathbf{r}', \quad \text{Eq. 1}$$

where \mathbf{r} and \mathbf{r}' are three-dimensional vectors in image and object reference spaces, respectively.

If the activity $f(\mathbf{r})$ is considered to be distributed over N functionally distinct tissue components of true activity concentra-

Received Sep. 16, 1996; revision accepted Aug. 5, 1997.

For correspondence or reprints contact: Olivier Rousset, PhD, McConnell Brain Imaging Center, Montréal Neurological Institute, 3801 University Street, Montréal H3A-2B4, Québec, Canada.

tion T_i , each defined over a spatial domain D_i , Equation 1 can be written as:

$$g(r) = \sum_{i=1}^N \int_{D_i} T_i(r') h(r, r') dr'. \quad \text{Eq. 2}$$

Because $T_i(r)$ is considered to be constant over D_i (i.e., homogeneous activity distribution within each tissue component), Equation 2 becomes:

$$g(r) = \sum_{i=1}^N T_i \int_{D_i} h(r, r') dr'. \quad \text{Eq. 3}$$

The integration of the system's PSF $h(r)$ over D_i represents the regional spread function (RSF) of tissue domain D_i , assuming a unit activity distribution:

$$\text{RSF}_i(r) = \int_{D_i} h(r, r') dr'. \quad \text{Eq. 4}$$

In principle, to correct for partial volume averaging of voxels with different activity, we could consider each voxel as functionally unique and perform a full three-dimensional "deconvolution" of the PET image with the inverse of the system response function. Although this is acceptable conceptually, it is impractical due to the resultant noise amplification, as well as its high computational cost.

If one seeks to solve the imaging equation (Eq. 3) for the true activity concentrations (T_i), it is only when one isolated tissue component taking up the tracer is considered (i.e., $n = 1$) that the problem can be solved directly. In this case, the corrected image becomes a simple division of the observed PET image by the tissue component's response function $\text{RSF}_i(r)$. This has been done with correction for dilution of brain matter activity by tracer-free CSF spaces (19,20). When $n = 2$ (e.g., gray and white matter regions), there must be an a priori assessment of one of the two unknowns, as in the method presented by Müller-Gärtner et al. (21). These authors identified "true" white matter as a remote large white matter region, in which resolution effects were considered negligible due to its relatively large cross-section; they assumed white matter activity to be uniform throughout the brain. However, when the distribution of activity is considered to be more heterogeneous (i.e., $n > 2$), it becomes increasingly difficult to account for the contamination from a tissue component suffering from PVEs itself. For instance, to account for activity spilled over from cortical gray matter into a subcortical nucleus such as the amygdala (22), true cortical gray activity is assessed from the more global gray matter-PET image (21) and is assumed to reflect the activity of gray matter regions actually contaminating the amygdala, without being itself contaminated by the amygdala or other adjacent structures.

Instead of considering the whole PET image for signal recovery, we can restrict the domain of calculation of the PSF convolution with the true objects to the limited area that constitutes a region of interest (ROI). The mean value observed within ROI_j , is then given by:

$$t_j = \frac{1}{n_{\text{pix}}} \sum_{i=1}^N T_i \int_{\text{ROI}_j} \text{RSF}_i(r) dr, \quad \text{Eq. 5}$$

where n_{pix} is the number of pixels in ROI_j .

Equation 5 can be reexpressed as:

$$t_j = \sum_{i=1}^N \omega_{ij} T_i, \quad \text{Eq. 6}$$

$$\omega_{ij} = \frac{1}{n_{\text{pix}}} \int_{\text{ROI}_j} \text{RSF}_i(r) dr. \quad \text{Eq. 7}$$

The weighting factors ω_{ij} represent the contribution of each domain D_i to any ROI_j of the image and can be computed for each component of nonzero activity to generate a matrix of regional transfer coefficients:

$$\begin{bmatrix} t_1 \\ t_2 \\ \vdots \\ t_N \end{bmatrix} = \begin{bmatrix} \omega_{11} & \omega_{21} & \cdots & \omega_{N1} \\ \omega_{12} & \omega_{22} & & \vdots \\ \vdots & & \ddots & \vdots \\ \omega_{1N} & \omega_{2N} & \vdots & \omega_{NN} \end{bmatrix} \times \begin{bmatrix} T_1 \\ T_2 \\ \vdots \\ T_N \end{bmatrix}. \quad \text{Eq. 8}$$

The regional values actually observed with PET, t_j , and this known regional geometric transfer matrix (GTM) represent a system of linear equations that can be solved for the true values T_i . While the diagonal terms of this matrix represent tissue self-interaction (regional RC), the off-diagonal terms ω_{ij} ($i \neq j$) express the fraction of true activity T_i spilled over from domain D_i and integrated in ROI_j .

Accuracy Versus Precision

Although the calculation of the inverse matrix and determination of the corrected values T_i are straightforward, such inversion procedures tend to increase the noise present in the corrected estimates. Exact determination of the noise amplification requires knowledge of the covariance structure of the GTM (23).

However, the error attached to the corrected value T_i , in terms of its s.d. dT_i , cannot exceed that obtained in the case of independent variables:

$$dT_i^2 \leq \sum_{j=1}^N \left(\frac{\partial T_i}{\partial t_j} dt_j \right)^2 = \sum_{j=1}^N (\omega'_{ij} dt_j)^2, \quad \text{Eq. 9}$$

where ω'_{ij} are the elements of the inverse of the GTM given in Equation 8, and dt_j represents the s.d. attached to the observed value t_j . An initial estimate of the noise enhancement phenomenon introduced by the correction process can be derived from Equation 9, which represents an upper bound. We define the noise magnification factor (NMF), as the ratio of the coefficients of variation (COVs) after and before PVC:

$$\text{NMF} = \frac{dT_i/T_i}{dt_i/t_i}. \quad \text{Eq. 10}$$

By multiplying numerator and denominator by the true activity T_i , the expression of the NMF becomes:

$$\text{NMF} = \frac{dT_i}{dt_i} \times \frac{t_i}{T_i} \times \frac{T_i}{T_i} = \frac{dT_i}{dt_i} \times \frac{\text{ARC}_{\text{obs}}}{\text{ARC}_{\text{cor}}} \quad [0 < \text{ARC} < 1] \quad \text{Eq. 11A}$$

and

$$\text{NMF} = \frac{dT_i}{dt_i} \times \frac{1 - |\text{ARC}_{\text{obs}} - 1|}{1 - |\text{ARC}_{\text{cor}} - 1|} \quad [\text{ARC} > 0], \quad \text{Eq. 11B}$$

where ARC is the apparent RC (8), which represents the ratio of regional-to-true (T) activity concentrations before ($\text{ARC}_{\text{obs}} = t_i/T$) and after ($\text{ARC}_{\text{cor}} = T_i/T$) PVC. In most cases, ARC has a value smaller than 1, and the NMF can be simply expressed, as in

Equation 11A, as the product of the corrected-to-observed precision ratio (dt_i/dt_i) and the observed-to-corrected accuracy ratio (ARC_{obs}/ARC_{cor}). However, the general expression valid for any value of ARC is given by Equation 11B.

Implementation

Magnetic Resonance Imaging-Based Model of the Brain. With the advent of new multimodality image registration techniques (24,25), the brain anatomy and its underlying tracer uptake can be accurately spatially aligned in three dimensions. To create a model of the brain providing the structural information necessary for PVC, high-resolution volumetric MR data are collected using a three-dimensional gradient-echo sequence (typically TE = 10 ms, TR = 18ms, NEX = 1, flip angle = 30°) and registered with the corresponding PET data using a three-dimensional landmark-matching algorithm (26). The registered MRI volume is then resampled to thin (1- to 2-mm) slices and processed through a three-dimensional tissue classifier (27) to segment the object into its main components, (e.g., gray matter, white matter and CSF). In addition, because tissue classifiers are unsuitable for discriminating between components exhibiting similar signal intensity with MRI, (e.g., distinguishing subcortical from cortical gray matter regions), the boundaries of such structures are manually outlined from consecutive MR slices covering the specific brain region. Their three-dimensional shape is then built up from the stack of two-dimensional ROIs to create volumes of interest (8,26,28). The resulting fully labeled MRI volume is then assigned with tracer concentrations representing true activity distributions, assuming uniform uptake within each identified tissue or regional component.

PET Simulation. The PVC algorithm makes use of an analytical three-dimensional PET simulator developed by our group, which incorporates all the major physical and statistical effects that are inherent in PET data acquisition and reconstruction (29,30). The various components of the previously labeled MRI volume are assigned with radioactivity concentrations, and the resulting idealized activity distribution is sampled according to the geometry of our PC-2048 PET scanner (Eq. 4). A spatially invariant three-dimensional Gaussian function was used to approximate the three-dimensional PSF of the tomograph. The true axial resolution of the PC-2048 is 6.1 mm FWHM, whereas the transverse resolution ranges from 4.6 mm at the center of the FOV to 6.4 at a radius of 9 cm (31). Because more of the FOV falls at larger distance from the center, an annular-weighted average value for transverse resolution is close to 6 mm. Therefore, we selected a Gaussian function of 6 mm FWHM in all three directions. The property of separability of the PET imaging system allows us to simulate three-dimensional resolution effects by first convolving the activity distribution in the axial direction with a one-dimensional Gaussian function (6 mm FWHM), which models the axial aperture function of the scanner (i.e., slice thickness). Idealized projections sinograms (32) of each axially smoothed slice are computed with radial and angular sampling of the scanner, e.g., 128 elements \times 128 angles \times 2 mm ray geometry for the PC-2048. The resulting projection profiles are then convolved with a one-dimensional Gaussian function (6 mm FWHM) to model the transverse detector response function. Other physical effects inherent to PET data acquisition such as photon attenuation or scatter counts can be included at the sinogram level to produce noisy PET-like images.

Regional Spread Function and Geometric Transfer Matrix. To characterize the PET response to the object $f(r)$, the different tissue domains D_i identified in the coded MRI volume are processed separately through the PET simulator. The tissue domain D_i assigned with unit activity is convolved with the three-dimensional

PSF of the scanner as described above. The simulated sinogram is then reconstructed by use of the tomograph's filtered back-projection algorithm, ensuring the same amount of image degradation resulting from projection filtering and backprojection (33). The resulting image then represents the response function of the scanner to component D_i , i.e., $RSF_i(r)$ (Eq. 4).

Each GTM coefficient ω_{ij} is then calculated (Eq. 7) as the proportion of the total $RSF_i(r)$ image density (integrated over all pixels in the image volume) within the ROI_{*j*} boundary (integrated over all ROI pixels).

Experiment I: Sphere Phantom

To validate the accuracy of the simulated PSF of the tomograph, we used a water-filled 20-cm-diameter cylinder containing six hollow spheres with inner diameters ranging from 4.0 to 15.5 mm. All the spheres were filled with a uniform concentration of ^{68}Ga (half-life = 1.14 hr) and scanned with their equator aligned with one of the rings of the PET scanner. Activity concentration at beginning of scan was 208 $\text{kBq}\cdot\text{ml}^{-1}$, and 2 million events were collected. Images were reconstructed with a 5 mm FWHM ramp filter, after correction for attenuation using a transmission ^{68}Ga rod source and for scatter counts using a one-dimensional deconvolution kernel on projection data. A simulated version of this phantom was then created that had geometrical dimensions and configuration identical to those of the physical phantom and consisted of 2-mm-thick stacked disks cut from numerical sphere models. This procedure was designed to avoid the potential error in object size that could have been introduced by the segmentation process. Because we were only interested in relative intensity, an arbitrary activity concentration was assigned to the sphere model, and the correct noise level was set by simulating the acquisition of a total of 2 million counts, similar to that recorded during the real PET experiment. Recovery coefficients were calculated for each sphere using maximum pixels and compared with theoretical values computed from the Gaussian integral over a spherical region of space (3).

Experiment II: Physical Brain Phantom

For validation in a more realistic setting, a plastic model of the brain provided by Dr. Dean Wong of Johns Hopkins University (Baltimore, MD) was used. The design of the brain phantom is based on digitized brain slices and is intended to estimate partial volume losses in neuroreceptor studies (34). The model consists of separately fillable plastic cavities, representing the basal ganglia of the human brain, and plain polyester resin models of ventricular spaces, located in a main fillable chamber simulating the rest of the brain, all surrounded by a human skull (Fig. 1). Careful testing of the phantom structural integrity indicated that the left caudate nucleus (CN) and the left globus pallidus (GP) were damaged and open to the main cavity [background (BKG)]. Therefore, for these experiments, the left CN and left GP compartments were filled with the same solution as the BKG. Although the left putamen (PU) appeared to be structurally intact, its proximity to the damaged left CN and left GP compartments motivated our decision not to fill it with radioactive solution that might leak. Instead, the left PU compartment was filled with water and treated as part of the ventricular compartment.

Static Tracer Distribution. The phantom was centered in the PC-2048 PET scanner and underwent a transmission scan to account for photon attenuation. The brain phantom was then filled with a solution of ^{18}F -fluorodeoxyglucose (FDG) at two different concentrations, one for the small cavities (61 $\text{kBq}\cdot\text{ml}^{-1}$) and one for the main chamber (16 $\text{kBq}\cdot\text{ml}^{-1}$). The PET acquisition protocol was typical of F-DOPA studies (35) and was as follows: six 30-sec, seven 1-min, five 2-min, four 5-min and five 10-min frames. Samples were taken from the radioactive solutions and measured

TABLE 1

Regional Transfer Coefficients of the Geometric Transfer Matrix

Observed regional activity	Integration of true activity concentration* %			
	CN	PU	BKG	GP
CN	67.24	1.77	23.32	0.84
PU	3.70	48.28	35.79	11.17
BKG	0.00	0.02	98.92	0.00
GP	2.15	7.04	25.80	61.14

*Shown is the percentage integration of true activity concentration in selected regions into the observed regional activity in the same selected regions.

CN = caudate nucleus; PU = putamen; BKG = background; GP = globus pallidus; GTM = geometric transfer matrix; RSF = regional spread function.

The GTM was obtained from RSF images and ROI templates shown in Figure 2. The GTM is dependent on geometrical relationships between the structures of interest and on the ROIs and image resolution used but is independent of tracer activity distribution at any time. Note that, for a given structure, the sum of its regional transfer coefficients ω_{ij} is always smaller than 1 due to dilution of activity in nonradioactive regions (e.g., ventricles).

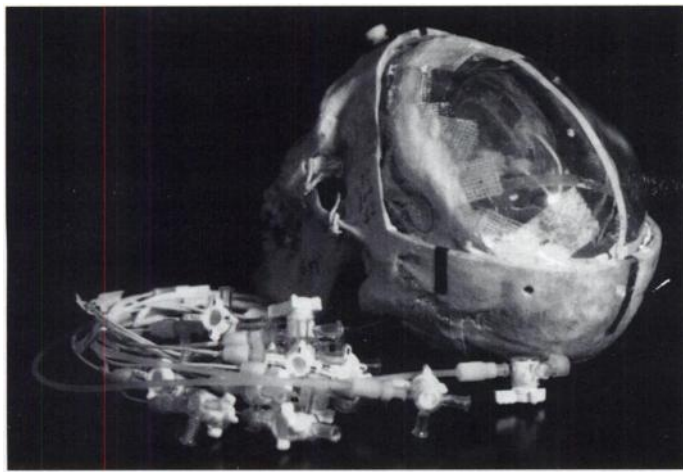


FIGURE 1. Physical brain phantom with "top" removed, unveiling a plastic model of the brain embedded in a dried skull. Independently fillable cavities in the shape of the striatum allowed for the assessment of the performance of the PVC algorithm in conditions representative to PET radioligand studies.

with a cross-calibrated well counter to provide the true isotope concentrations. Images were reconstructed using a 6 mm FWHM Hanning filter, after correction for photon attenuation, as well as random and scatter counts. Subsequently, a typical T1-weighted sequence of the phantom was acquired on an MRI unit (General Electric, Milwaukee, WI, 1.5 T), with the deep cavities filled with copper sulfate solution ($\text{CuSO}_4^{2-} \cdot 5\text{H}_2\text{O}$, 0.1 mM) to provide sufficient image contrast for further "tissue classification." The volumetric MRI dataset was registered with the high-resolution 15-slice PET volume obtained by summing all dynamic frames. The MRI volume was resampled to 2-mm-thick images (26) and segmented into its various compartments, i.e., CN, PU, GP, ventricles and main chamber (BKG). The finite wall thickness of the phantom compartments was explicitly dealt with by including in the simulation a 1-mm-thick boundary region around each active compartment. Apparent regional concentrations within four PET slices of the phantom were measured using MRI-based ROIs for each compartment with nonzero activity. Simulated images of each component were then generated to obtain RSF images (Fig. 2), and the GTM for the particular ROI template and slice was extracted (Table 1). The observed regional values were then corrected according to the estimated GTM (Eq. 8), considering either a three-

or a four-tissue system, i.e., with or without CN, PU, BKG, GP (Fig. 2), depending on the slice analyzed. We could equally have chosen to perform a 2×2 correction instead of a 3×3 or 4×4 because the three small cavities contained the same concentration of radioactivity and could be regarded as a single region. These spaces were treated as separate compartments to evaluate the cross-contamination factors, as would be the case if the tracer distribution in each of the CN, PU and GP compartments was different.

Analysis of the images collected with different total counts also allowed for the study of statistical error in the measured mean regional values at varying noise conditions. The relative degradation of precision was assessed via the dispersion of the observed (corrected) regional values with respect to the mean observed (corrected) data over the entire time series. These values were compared with maximum expectations derived from Equations 9–11B.

Dual-Isotope Experiment. To investigate further PVC performance with a different scanner geometry and changing tracer contrast, the phantom was scanned with the PC-4096 system installed at Johns Hopkins. The major different physical characteristic to be accounted for between this system and that at the Montréal Neurological Institute was the number of detectors (512 instead of 256). Magnetic resonance data were acquired on a General Electric SIGNA 1.5-T unit using a spoiled gradient-recalled acquisition in the steady-state sequence (TE = 5 ms, TR = 35 ms, NEX = 2, flip angle = 45°) and stored as a matrix of $256 \times 256 \times 192$, with a pixel size of 0.94 mm.

To simulate different tracer kinetics, a dual-isotope phantom experiment was performed (11). Both the right CN and PU compartments were filled with an aqueous solution of ^{18}F (half-life = 110 min), whereas the main chamber was filled with a ^{11}C solution (half-life = 20 min). To further complicate the distribution of activity within the phantom, the GP compartment was filled with a mixed solution of the two isotopes. Starting concentrations were $74 \text{ kBq}\cdot\text{ml}^{-1}$ for ^{11}C and $51.8 \text{ kBq}\cdot\text{ml}^{-1}$ for ^{18}F . The phantom was scanned for 85 min (~ 4 ^{11}C half-lives), providing a series of 60-sec frames interleaved with two short series of 15-sec frames (one at 10 min and the other at 45 min), to obtain noisier data. Time-activity curves were derived from each structure on one PET slice from a total of 100 reconstructed images without radioisotope decay correction. The same procedures of simulation described above

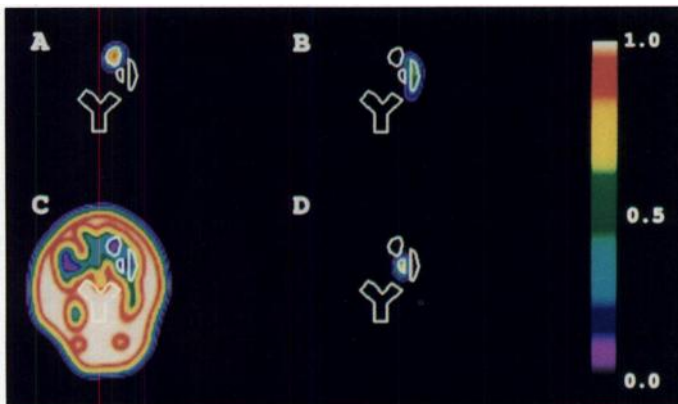


FIGURE 2. Extraction of the GTM in the case of the physical brain phantom. The RSF image of each compartment, right CN (A), right PU (B), main cavity BKG (C) and right GP (D), is generated by assigning unit activity to the corresponding tissue map identified from MR images and processed through the PET simulator. After application of the user-defined ROI template normally used for extracting regional tracer concentrations, each RSF image provides a column of the GTM, the elements of which represent the fraction of true activity of the tissue in each user-defined ROI. Images were reconstructed at a resolution of 6 mm FWHM.

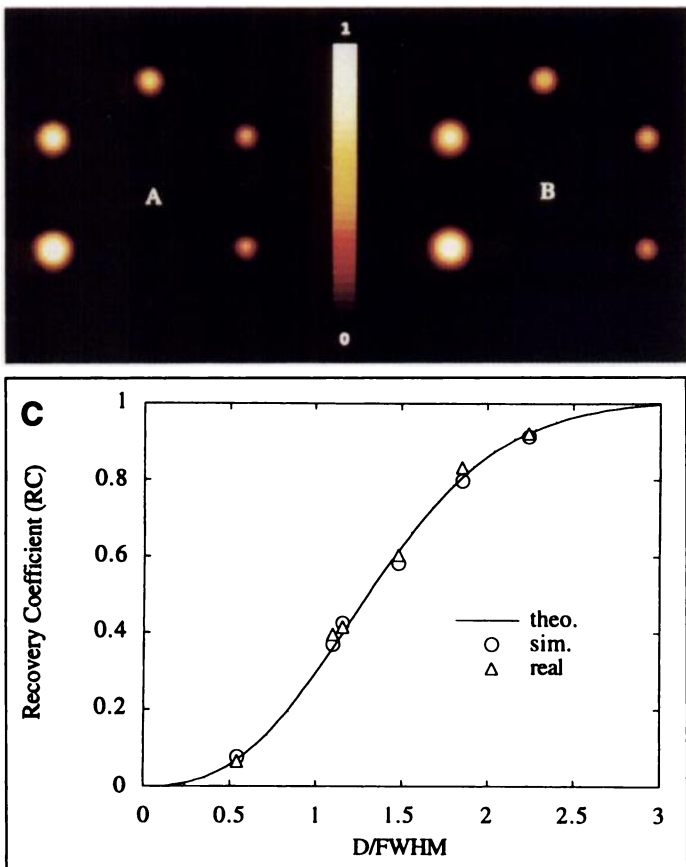


FIGURE 3. Real (A) and simulated (B) images of a set of six spheres of 4.0-, 7.5-, 8.5-, 11.0-, 13.0- and 15.5-mm diameters. These images were reconstructed with a 5-mm FWHM Ramp filter. Note that the smallest sphere remains practically invisible for both real and simulated cases. (C) RCs as a function of sphere diameter normalized to the image resolution. The solid line is the theoretical integral of a Gaussian over a spherical region of space (3).

were applied to provide a GTM characteristic of the geometric conditions of the experiment. Both observed and corrected TACs were fitted with monoexponential functions to derive the half-life of both tracers. To estimate the accuracy of the physical half-life of the tracer before/after PVC for various image resolutions, the analysis was repeated for different values of reconstruction filter width.

RESULTS

Experiment I: Sphere Phantom

Figure 3A and B, compares sphere phantom images from real

data and simulation. The RC values corresponding to the ratio of the peak value (i.e., 5-pixel ROI) observed in the image to the actual isotope concentration are plotted versus the sphere diameter normalized to the FWHM of the system PSF (Fig. 3C). Both simulated and real data agree with theoretical calculations (3) within 2%.

Experiment II: Physical Brain Phantom

Static Tracer Distribution. A typical GTM obtained for the PET slice in which all three small cavities were visible is presented in Table 1. For instance, at a resolution of 6 mm FWHM, the estimated regional concentration of the caudate cavity (CN) contains 67% of its own true activity (true RC), 23% of true activity of the main cavity (BKG) and 1.8% and 0.8% of PU and GP true isotope concentrations, respectively (Table 1). The fractions of contamination (off-diagonal terms of the GTM) might be slightly underestimated compared to structures of comparable size in the brain due to the wall thickness of the small cavities acting like an extra tracer-free space separating the small cavities from each other and from the main compartment.

The principal results on the accuracy of the regional activity estimates before and after PVC are summarized in Table 2. Reported values are mean \pm s.d. for the series of 27 images, with the number of counts per slice ranging from 52,000 to 1.1 million. The recovery factors for the observed values were in the range of 59%–72% for CN, 54%–77% for PU and 75% for GP, which was contained in a single slice. The values for the “volume” measurement were obtained after weighted averaging of the mean activities from individual ROIs by their respective area over four contiguous PET slices (Fig. 4) and were 67.6% \pm 1.5% for CN and 70.1% \pm 0.6% for PU. Partial volume-corrected estimates were in the range of 95%–106% of true value for CN and 91%–107% for PU. The analysis of all four slices provided an average estimate of ARC after PVC of 98.5% \pm 2.4% for CN and 97.3% \pm 1.1% for PU. For the GP compartment, 96% recovery was achieved in the single slice analyzed (Table 2).

The root mean-square deviations from the mean observed values were relatively low over the entire time series (<4%; Table 2). As expected, the fluctuations around the mean regional values for similar number of accumulated counts were more pronounced for lower statistics (Fig. 5). The NMF, defined as the ratio of COV after and before PVC, was estimated experimentally from the mean regional activity values and their precision obtained from the analysis of regional TACs (Table 2). The values of the NMF for the small cavities

TABLE 2
Apparent Recovery Coefficients in Different Compartments of the Physical Brain Phantom

	Slice				Volume
	1	2	3	4	
Caudate nucleus					
Observed	69.4 \pm 2.6	72.4 \pm 2.5	66.8 \pm 1.9	58.9 \pm 2.2	67.6 \pm 1.5
Corrected	98.2 \pm 4.3	94.7 \pm 3.8	97.7 \pm 2.9	106.2 \pm 5.0	98.5 \pm 2.4
Putamen					
Observed	54.1 \pm 3.3	75.2 \pm 2.5	77.3 \pm 1.5	63.5 \pm 1.5	70.0 \pm 0.6
Corrected	94.5 \pm 10.7	107.3 \pm 5.2	98.0 \pm 2.4	90.6 \pm 2.5	97.3 \pm 1.1
Globus pallidus					
Observed		75.0 \pm 2.4			
Corrected		96.1 \pm 3.9			
Background					
Observed	97.0 \pm 2.9	97.3 \pm 4.4	101.1 \pm 2.4	104.9 \pm 2.5	100.0 \pm 1.7
Corrected	97.5 \pm 2.9	98.3 \pm 4.4	101.6 \pm 2.4	105.5 \pm 2.5	100.6 \pm 1.7

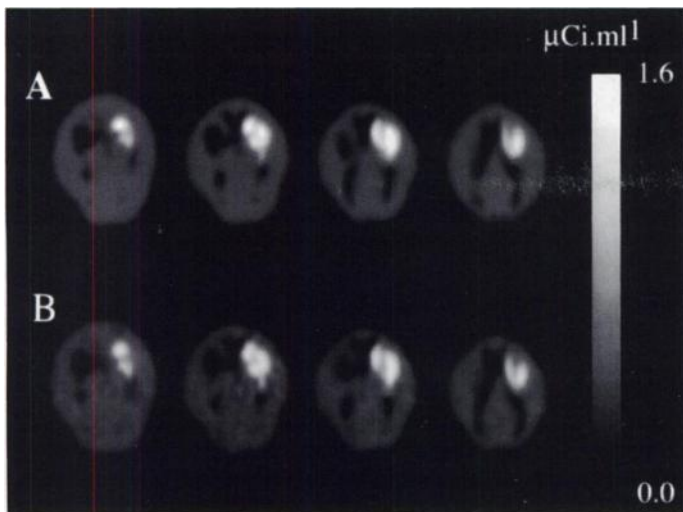


FIGURE 4. Real (A) and simulated (B) contiguous PET slices (6.5 mm apart) of the physical brain phantom filled with ^{18}F FDG. Simulated images were generated after assigning corrected values to each compartment of the phantom identified from MRI and after simulation of all the physical effects inherent in PET data acquisition and reconstruction. Photon attenuation was accounted for by generating attenuation profiles of the real PET transmission image, assuming that the phantom was essentially constituted of a water-like attenuating medium, with a mean attenuation coefficients of 0.096 cm^{-1} . The images contain around 5 million counts each and were reconstructed with a 6-mm Hanning filter.

of the brain phantom are reported in Table 3, together with maximum expectations derived from Equations 9–11B. They were found to vary across slices from 1.07 to 1.24 for CN and from 1.21 to 1.84 for PU. In the case of GP, we observed a 27% increase of the COV (i.e., $\text{NMF} = 1.27$) compared to a maximum theoretical value of 1.29.

Dual-Isotope Experiment. The least squares fitting of the uncorrected TACs extracted from the deep nuclei filled with ^{18}F shows a recovery of half-life of 80% for CN and 70% for PU at the best resolution (Table 4). Partial volume-corrected estimates of the tracer's half-life were within 2.5% of true value, with a precision similar to that of observed values (Table 4). The analysis of TACs from the GP compartment filled with a

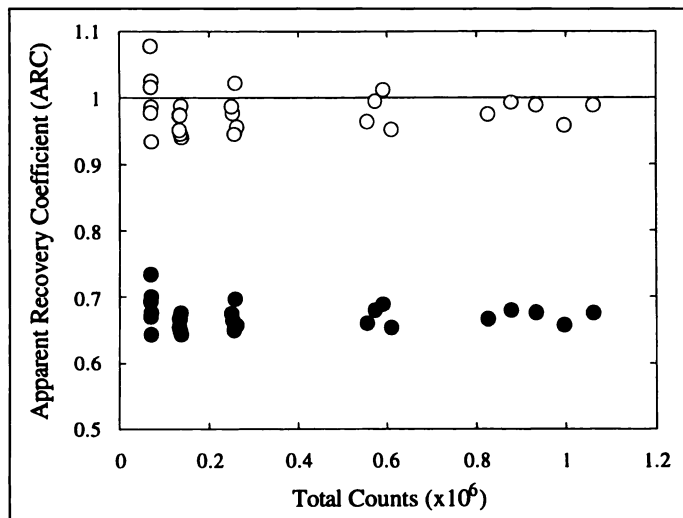


FIGURE 5. Apparent RCs (ARCs) of observed (●) and corrected (○) regional concentrations obtained in the compartment of the phantom representing the right PU. These data were obtained for one single PET slice for images of various length and show an underestimation of tracer concentration in the small cavity, whereas good accuracy is achieved for the corrected estimates (see Table 2 for more results). Because of Poisson statistics, we note a greater fluctuation of the data at low accumulated counts.

TABLE 3
Noise Magnification Factor for the Basal Ganglia

Cavity	Slice				Volume
	1	2	3	4	
Caudate nucleus					
Actual*	1.17	1.17	1.07	1.24	1.12
Theory†	1.29	1.22	1.10	1.27	
Putamen					
Actual*	1.84	1.44	1.21	1.23	1.25
Theory†	2.07	1.72	1.25	1.28	

* Derived from the analysis of the precision of corrected versus observed TACs.

†Maximum theoretical values derived from Equations 9–11B.

mixture of ^{11}C and ^{18}F solutions could not be completed: small dimensions of GP and poor image statistics made it impossible to fit the present data. Raw data from GP were nonetheless incorporated for the correction of the other compartments.

An example of distorted TACs for deep nuclei consequent to spillover from the faster kinetics of the main compartment (filled with ^{11}C) is shown in Figure 6, together with its recovery after PVC. Figure 7 depicts the influence of image resolution on quantitation of kinetic parameters. Observed estimates of fluorine half-life were decreased a further 14% of the true value when the filter size used during image reconstruction was increased from 6 mm to 12 mm FWHM. Under the same conditions, we observed an overestimation of tracer's half-life of only 1.3% for CN and 4.7% for PU after PVC (Fig. 7).

DISCUSSION

Accuracy

Provided that the GTM is not singular, the set of linear equations (Eq. 5) can be solved directly for the true regional values by matrix inversion (36). The accuracy of the elements of the inverse GTM (i.e., correction factors) depends on the degree of ill-conditioning of the GTM and could be studied after precise determination of the error matrix associated with the computation of the GTM. However, the results indicate that the PVC algorithm is capable of accurately providing corrected activity concentrations of small activity distributions surrounded by a warm background (Table 2).

The dual-isotope experiment clearly demonstrated the capability of PVC to accurately restore the shape of TACs distorted by the presence of surrounding activity with different kinetics (Table 4 and Fig. 6). Although we observed a linear degradation of tracer's half-life with respect to image resolution, corrected values were only slightly overestimated as the resolution degrades (Fig. 7).

The accuracy of the PVC method depends primarily on the proper identification of the tissues believed to have different functional properties. In the case of the brain phantom data presented here, a nearly complete recovery was achieved. In the case of human data, it is more difficult to evaluate the accuracy of the algorithm used to identify brain tissue components. Improved methods are now being developed for both tissue classification (37) and regional labeling in MRI volumes (38). These tools automate the segmentation process and reduce potential variability due to human error. Another source of error is a potential misregistration between PET and MRI data. We have previously reported an error on the order of 5% of true activity per mm of axial misregistration (10).

TABLE 4
Recovery of Half-Life Characteristics of the Tracers (Image = 6 mm FWHM)

Structure	Tracer	Observed			Corrected		
		T _{1/2} (min)	Recovery* (%)	Root mean-square (%)	T _{1/2} (min)	Recovery* (%)	Root mean-square† (%)
Caudate nucleus	¹⁸ F	89.4	81.3	6.2	112.3	102.5	7.0
Putamen	¹⁸ F	76.8	69.8	4.1	109.6	100.0	4.2
Background	¹¹ C	20.1	98.5	1.1	20.1	98.5	1.2

* Percentage of true tracer half-life value (T_{1/2} = 109.6 min for ¹⁸F and 20.4 min for ¹¹C).

† Mean root mean-square error between data points and the fitting curve.

Precision

The analysis of the COV of the regional estimates, before and after PVC, allowed the assessment of the degradation of data precision. Our results gave an initial estimation of precision depreciation inherent in PVC and proved to be reasonable in noise conditions typical of human brain studies (Table 3). Although the actual NMF involves the estimate of the covariance matrix (23), the maximum degradation of data precision due to the noise-amplification phenomenon can be easily predicted (Eqs. 9–11B). This can provide a guideline for the best trade-off between parameters involved in the precision of observed measurements, such as time sampling strategy, amount of smoothing introduced during image reconstruction and ROI characteristics. In addition, the opportunity to perform a three-dimensional analysis/correction (i.e., averaging across PET slices) allows the limitation of noise propagation (Table 3), while providing a high degree of accuracy (Table 2).

Although the PVC method is presented to correct regional measurements, it could also be applied on a pixel-by-pixel basis, reducing the size of the ROIs to that of a pixel. This approach requires very intensive computation, and the resulting

noise amplification would likely become unacceptable. The more practical method presented here provides regional concentration values corrected for the PVEs at a low computational cost. Most importantly, this algorithm is robust to noise propagation during the correction process.

In the current PVC algorithm, activity distribution within each structure is assumed to be uniform. However, our method can be applied to brain models accounting for tracer inhomogeneity. Such models can be created based on postmortem brain data or probabilistic brain atlases (39). In addition, we are incorporating spatially variant three-dimensional PSFs in the PET simulation program to compensate for nonuniform resolution effects (2).

CONCLUSION

The PVC algorithm is based on the principles of linear systems and pairwise interaction between identifiable regions containing homogeneous radioactivity concentrations. Rather than subtracting contaminating activity coming from adjacent tissue for which one needs to estimate the true activity, we estimate the contribution of each functional tissue to a particular ROI. By characterizing the signal interaction between structures on a ROI basis, independently from image activity, the method allows for the simultaneous correction of any number of identified tissue TACs. We have proved in this work based on phantom studies that the PVC algorithm was capable of providing accurate corrected regional concentration within small structures such as the human basal ganglia. Furthermore,

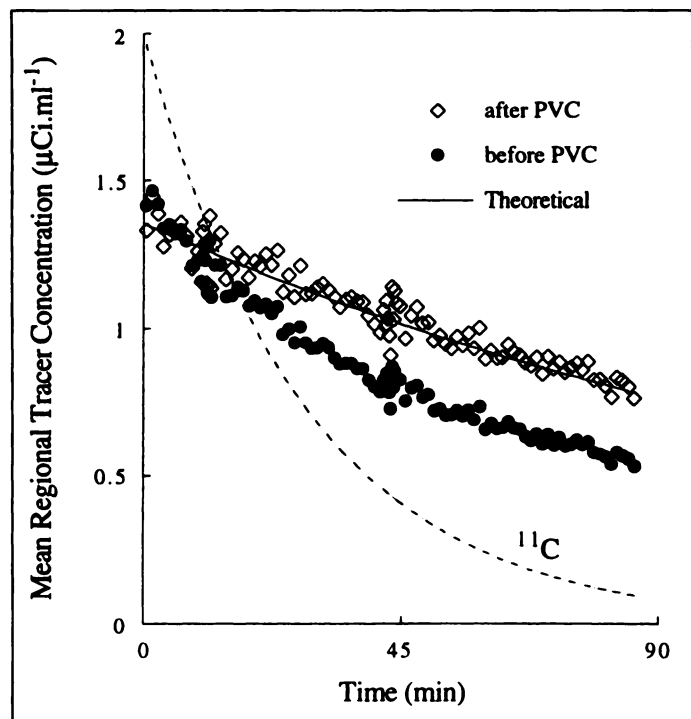


FIGURE 6. Time-activity curves obtained from the regional estimate of the PU activity over the series of non-decay-corrected images, before and after PVC, compared to the theoretical TAC of ¹⁸F derived from the initial true concentration and the tracer's half-life. The theoretical TAC from the main compartment (BKG) is also represented (¹¹C curve) to demonstrate prevailing contrast at each time point.

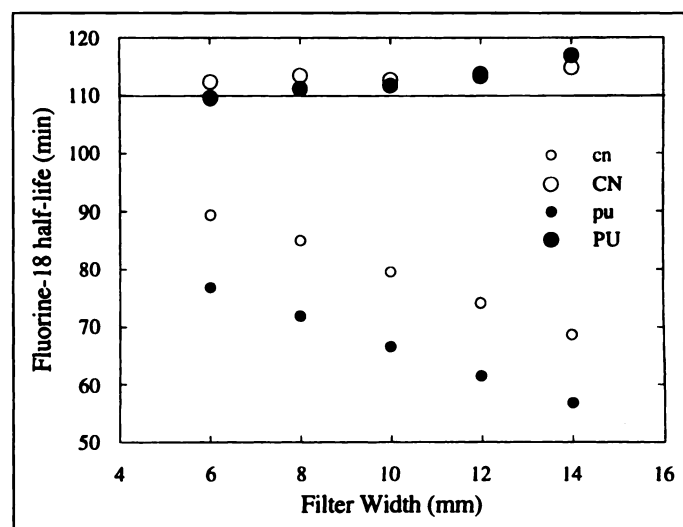


FIGURE 7. Accuracy of tracer's half-life for various image resolution values obtained for the basal ganglia structures. Note the linear underestimation of ¹⁸F's half-life derived from the observed TACs for the CN (cn) and PU (pu) when the width of the filter was increased in image reconstruction, whereas accurate and steady estimates were achieved after PVC (CN and PU curves).

the propagation of statistical noise during PVC was found to be easily predictable and suitable for application in dynamic PET. In conclusion, PVC can be applied to any PET studies in which a functional segmentation specific to the tracer is available. This would be of particular use for metabolic and neuroreceptor studies of normal human brain and of brain disorders because it could provide new insights and perspectives into what PET images are really telling us.

ACKNOWLEDGMENTS

Special thanks to the staff at the cyclotron units of the Montreal Neurological Institute and The Johns Hopkins Medical Institution for the production of radioisotopes used in the phantom experiments. We also thank Dean Wong for providing the brain phantom, as well as Sylvain Milot and Stefano Marengo for helpful technical assistance. This work was supported by Medical Research Council (Canada) grant SP 30 and by the Conseil Régional Rhône-Alpes (France).

REFERENCES

- Hoffman EJ, Huang SC, Phelps ME. Quantitation in positron emission tomography: 1. Effect of object size. *J Comput Assist Tomogr* 1979;3:299–308.
- Hoffman EJ, Huang SC, Plummer D, Phelps ME. Quantitation in positron emission computed tomography: 6. Effect of nonuniform resolution. *J Comput Assist Tomogr* 1982;5:987–999.
- Kessler RM, Ellis JR, Eden M. Analysis of emission tomographic scan data: limitations imposed by resolution and background. *J Comput Assist Tomogr* 1984;3:514–522.
- Brooks RA, Chiro GD. Principles of computer assisted tomography (CAT). *Phys Med Biol* 1976;21:689–732.
- Mazziotta JC, Phelps ME, Plummer D, Kuhl DE. Quantitation in positron emission tomography: 5. Physical-anatomical effects. *J Comput Assist Tomogr* 1981;5:734–743.
- Henze E, Huang SC, Ratib O, Hoffman E, Phelps ME, Schelbert HR. Measurement of regional tissue and blood-pool radiotracer concentrations from serial tomographic images of the heart. *J Nucl Med* 1983;24:987–996.
- Herrero P, Markham J, Bergmann SR. Quantitation of myocardial blood flow with $H_2^{15}O$ and positron emission tomography: assessment and error analysis of a mathematical approach. *J Comput Assist Tomogr* 1989;5:862–873.
- Rousset O, Ma Y, Kamber M, Evans AC. Three-dimensional simulations of radio tracer uptake in deep nuclei of human brain. *Comput Med Imaging Graphics* 1993;4/5:373–379.
- Links J, Zubieta J, Meltzer C, Stumpf M, Frost JJ. Influence of spatially heterogeneous background activity on “hot object” quantitation in brain emission computed tomography. *J Comput Assist Tomogr* 1996;4:680–687.
- Rousset OG, Ma Y, Léger GC, Gjedde AH, Evans AC. Correction for partial volume effects in PET using MRI-based 3D simulations of individual human brain metabolism. In: Uemura K, Lassen NA, Jones T, Kanno I, eds. *Quantification of brain function tracer kinetics and image analysis in brain PET*. Amsterdam: Elsevier Science; 1993:113–125.
- Cooke BE, Evans AC. A phantom to assess quantitative recovery of positron tomographs. *J Comput Assist Tomogr* 1983;5:876–880.
- Mullani NA. A phantom for quantitation of partial volume effects in ECT. *IEEE Trans Nucl Sci* 1989;36:983–987.
- Bendriem B, Dewey SL, Schlyer DJ, Wolf AP, Volkow ND. Quantitation of the human basal ganglia with positron emission tomography: a phantom study of the effect of contrast and axial positioning. *IEEE Trans Med Imag* 1991;10:216–221.
- Hoffman EJ, Cutler PD, Guerrero TM, Digby WM, Mazziotta JC. Assessment of accuracy of PET utilizing a 3-D phantom to simulate the activity distribution of [^{18}F]fluorodeoxyglucose uptake in the human brain. *J Cereb Blood Flow Metab* 1991;11:A17–A25.
- Phelps ME, Huang SC, Hoffman EJ, Plummer D, Carson RE. Analysis of signal amplification using small detectors in positron emission tomography. *J Comput Assist Tomogr* 1982;6:551–565.
- Hoffman EJ, Phelps ME. Positron emission tomography. Principles and quantitation. In: Phelps ME, Mazziotta JC, Schelbert HR, eds. *Positron emission tomography and autoradiography. Principles and applications for the brain and heart*. New York: Raven Press; 1986:237–286.
- Mahoney DK, Huang SC, Ricci AR, Mazziotta JC, Hoffman EJ, Phelps ME. A realistic computer-simulated brain phantom for evaluation of PET characteristics. *IEEE Trans Med Imag* 1987;6:250–257.
- Hutchins GD. Simulation of signal recovery in PET studies of cerebral physiology and biochemistry. In: Nagel JH, Smith WM, eds. *Proceedings of the 13th Annual International Conference IEEE-EMBS*. Piscataway, NJ: IEEE; 1991:215–216.
- Videen TO, Perlmutter JS, Mintun MA, Raichle ME. Regional correction of positron emission tomography data for the effects of cerebral atrophy. *J Cereb Blood Flow Metab* 1988;8:662–670.
- Meltzer CC, Leal JP, Mayberg HS, Wagner HN, Frost JJ. Correction of PET data for partial volume effects in human cerebral cortex by MR imaging. *J Comput Assist Tomogr* 1990;14:561–570.
- Müller-Gärtner H, Links J, LePrince JL, et al. Measurement of radiotracer concentration in brain gray matter using positron emission tomography: MRI-based correction for partial volume effects. *J Cereb Blood Flow Metab* 1992;12:571–583.
- Meltzer CD, Zubieta JK, Links JM, Brakeman P, Stumpf MJ, Frost JJ. MR-based correction of brain PET measurements for heterogeneous gray matter radioactivity distribution. *J Cereb Blood Flow Metab* 1996;16:650–658.
- Carson RE. A maximum likelihood method for region-of-interest evaluation in emission tomography. *J Comput Assist Tomogr* 1986;4:654–663.
- van den Elsen PA, Pol EJD, Viervgver MA. Medical image matching: a review with classification. *IEEE Eng Med Biol* 1993;12:26–39.
- Evans A. Correlative imaging. In: Wagner HN, Zabo Z, Buchanan JW, eds. *Principles of nuclear medicine*. Philadelphia: WB Saunders; 1995:405–421.
- Evans AC, Marrett S, Collins L. MRI-PET correlation in three dimensions using a volume-of-interest (VOI) atlas. *J Cereb Blood Flow Metab* 1991;2:A69–A78.
- Kamber M, Shinghal R, Collins DL, Franci GS, Evans AC. Model-based 3D segmentation of multiple sclerosis lesions in magnetic resonance brain images. *IEEE Trans Med Imag* 1995;3:442–453.
- Evans AC, Beil C, Marrett S, Thompson CJ, Hakim A. Anatomical-functional correlation using an adjustable MRI-based region of interest atlas with positron emission tomography. *J Cereb Blood Flow Metab* 1988;8:513–530.
- Ma Y, Kamber M, Evans AC. Three-dimensional simulation of PET brain images using segmented MRI and positron tomograph characteristics. *Comput Med Imaging Graphics* 1993;4/5:365–371.
- Ma Y, Evans AC. Analytical modeling of PET imaging with correlated functional and structural images. *IEEE Trans Nucl Sci* 1997:2439–2444.
- Evans AC, Thompson CJ, Marrett S, Meyer E, Mazza M. Performance evaluation of the PC-2048: a new 15-slice encoded-crystal PET scanner for neurological studies. *IEEE Trans Med Imag* 1991;2:A69–A78.
- Herman GT, Lewitt RM, Odhner D, Rowland SW. *Snark 89: a programming system for image reconstruction from projections*, publication no. MIPG160. Philadelphia: University of Pennsylvania; 1989.
- Spinks TJ, Guzzardi R, Bellina CR. Performance characteristics of a whole-body positron tomograph. *J Nucl Med* 1988;29:1833–1841.
- Wong DF, Links JM, Olliver M. An anatomically realistic brain phantom for quantification with positron tomography [Abstract]. *J Nucl Med* 1984;25:104.
- Kuwabara H, Cumming P, Reith J, et al. Human striatal L-DOPA decarboxylase activity estimated in vivo using 6- $[^{18}F]$ fluoro-DOPA and positron emission tomography. Error analysis and application to normal subjects. *J Cereb Blood Flow Metab* 1993;13:43–56.
- Dongarra JJ, Bunch JR, Moler CB, Stewart GW. *LINPACK user's guide*. Philadelphia: SIAM; 1979:1.7–1.21.
- Zijdenbos A, Evans AC, Riahi F, Sled J, Chui J, Kollokian V. Automatic quantification of multiple sclerosis lesion volume using stereotaxic space. In: Höhne K-H, Kikinis R, eds. *Proceedings of the 4th international conference on visualization in biomedical computing*. Berlin: Springer; 1996:439–448.
- Collins L, Holmes C, Peters TM, Evans AC. Automatic 3D segmentation of neuroanatomical structures from MRI. *Hum Brain Mapping* 1996;3:190–208.
- Evans A, Collins D, Holmes C. Automatic 3D regional MRI segmentation and statistical probability anatomy maps. In: Myers R, Cunningham V, Bailey D, Jones T, eds. *Quantification of brain function: tracer kinetics and image analysis in brain PET*. London: Academic Press; 1996:123–130.